

DEAD ZONE IN THE POLAR-CAP ACCELERATOR OF PULSARS

ALEXANDER Y. CHEN, ANDREI M. BELOBORODOV

Physics Department and Columbia Astrophysics Laboratory
 Columbia University, 538 West 120th Street New York, NY 10027

Draft version June 19, 2018

ABSTRACT

We study plasma flows above pulsar polar caps using time-dependent simulations of plasma particles in the self-consistent electric field. The flow behavior is controlled by the dimensionless parameter $\alpha = j/c\rho_{\text{GJ}}$ where j is the electric current density and ρ_{GJ} is the Goldreich-Julian charge density. The region of the polar cap where $0 < \alpha < 1$ is a “dead zone” — in this zone particle acceleration is inefficient and pair creation is not expected even for young, rapidly rotating pulsars. Pulsars with polar caps near the rotation axis are predicted to have a hollow-cone structure of radio emission, as the dead zone occupies the central part of the polar cap. Our results apply to charge-separated flows of electrons ($j < 0$) or ions ($j > 0$). In the latter case, we consider the possibility of a mixed flow consisting of different ion species, and observe the development of two-stream instability. The dead zone at the polar cap is essential for the development of an outer gap near the null surface $\rho_{\text{GJ}} = 0$.

Subject headings: plasmas — stars: magnetic fields, neutron

1. INTRODUCTION

Magnetic field lines that pass through the light cylinder of a rotating neutron star are twisted and carry electric currents $\mathbf{j}_B = (c/4\pi)\nabla \times \mathbf{B}$. These currents are sustained by electric field E_{\parallel} induced along the magnetic field \mathbf{B} , and ohmic dissipation $E_{\parallel}j$ feeds the observed pulsar activity. Voltage associated with E_{\parallel} controls the energies of accelerated particles, creation of secondary electron-positron pairs, and emission of radio waves. The accelerating voltage has been discussed in a number of works on pulsars beginning from early papers in the 1970s (Sturrock 1971; Ruderman & Sutherland 1975; Arons & Scharlemann 1979).

The key dimensionless parameter of the polar-cap accelerator is

$$\alpha = \frac{j_B}{c\rho_{\text{GJ}}}, \quad (1)$$

where $\rho_{\text{GJ}} = -\boldsymbol{\Omega} \cdot \mathbf{B}/2\pi c$ is the local corotation charge density of the magnetosphere (Goldreich & Julian 1969). For a special value of $\alpha = \alpha_0$ (close to unity) a steady state was found for the polar-cap flow with significant particle acceleration (e.g. Arons & Scharlemann 1979; Muslimov & Tsygan 1992). However, α is not, in general, expected to take this special value (e.g. Kennel et al. 1979). Global solutions for approximately force-free pulsar magnetospheres give α that significantly varies across the polar cap (Timokhin 2006). In general, α can take any value from $-\infty$ to $+\infty$, depending on the polar cap distance from the rotation axis and the location inside the polar-cap region.

The character of the polar-cap accelerator strongly depends on α (Mestel et al. 1985; Beloborodov 2008, hereafter B08). The steady solution with $\alpha = \alpha_0 \approx 1$ is a separatrix between two opposite regimes of efficient and inefficient acceleration.¹ In particular, if $0 < \alpha < 1$, E_{\parallel} is quickly screened in the charge-separated plasma flow-

ing from the polar-cap surface. The electric field satisfies Maxwell equations that read (in the co-rotating frame of the star, see e.g. Fawley et al. 1977; Levinson et al. 2005),

$$\nabla \cdot \mathbf{E} = 4\pi(\rho - \rho_{\text{GJ}}), \quad (2)$$

$$\frac{\partial \mathbf{E}}{\partial t} = 4\pi(\mathbf{j}_B - \mathbf{j}). \quad (3)$$

If $0 < \alpha < 1$, there exists a velocity $v = \alpha c$ that allows the charge-separated flow $j = \rho v$ to simultaneously satisfy $\rho = \rho_{\text{GJ}}$ and $j = j_B$. If the flow started from the conducting boundary (which has $E = 0$) with $v = \alpha c$, no electric field would be generated (then $\nabla \cdot \mathbf{E} = 0$ and $\partial \mathbf{E}/\partial t = 0$). The actual boundary has $v \neq \alpha c$, as charges are lifted from the polar-cap surface with a small initial v , comparable to the thermal velocity in the surface material. The deviation of v from αc implies $\rho \neq \rho_{\text{GJ}}$ or $j \neq j_B$, which generates electric field. B08 argued that Equations (2) and (3) with $0 < \alpha < 1$ always drive the flow toward $v = \alpha c$, like a pendulum is driven by gravity toward its equilibrium position. The resulting oscillations occur in space or time, according to Equations (2) or (3), respectively. For example, the steady-state solution for a cold flow exhibits oscillations in space (Mestel et al. 1985; B08). The oscillatory behavior of the flow with $0 < \alpha < 1$ is, in essence, Langmuir oscillations; they are generated near the boundary where the flow is injected with $v < \alpha c$ and accelerated toward $v = \alpha c$.

In this paper, we investigate the accelerator with $0 < \alpha < 1$ in more detail. In Section 2, we write down the steady-state solution for the charge-separated flow, generalized to non-zero temperature of the polar-cap. We argue that the flow is unstable to small perturbations and can develop into a complicated time-dependent state with a broad momentum distribution. To explore the behavior of the flow, we perform fully kinetic time-dependent simulations. The method of simulations is de-

(Muslimov & Tsygan 1992); its exact value is close to unity and is not essential for the rest of the paper.

¹ Hereafter we will refer to this separatrix as $\alpha = 1$, neglecting the deviation of α_0 from unity. The precise α_0 is controlled by the curvature of magnetic field lines and the general relativistic effects

scribed in Section 3, and the results are presented in Sections 4 and 5. Our simulations confirm the predicted turbulent Langmuir oscillations with a small voltage. Particle acceleration in the flow with $0 < \alpha < 1$ is insufficient to ignite pair creation. Implications of this “dead zone” for radio emission and outer gaps in pulsars are discussed in Section 6.

2. STEADY-STATE SOLUTION FOR A CHARGE-SEPARATED FLOW

2.1. Basic equations

It is natural first to attempt to construct a simple model assuming that the polar-cap flow is steady in the (rotating) frame of the neutron star. Given the steady magnetic field in this frame, and the steady boundary conditions at the stellar surface — excellent static conductor that can supply charges with a given temperature, — one could expect a steady state to be established unless the flow is prone to an instability.

Consider a charge-separated flow from the polar cap that carries electric current j_B along magnetic field \mathbf{B} . In a steady state $j = j_B$ (Equation 3). For simplicity, let us assume that \mathbf{B} is approximately perpendicular to the polar cap and let z measure the altitude above the stellar surface. A particle of mass m and charge e that starts with a Lorentz factor $\gamma_0 \approx 1$ at $z = 0$ will accelerate as it moves along the magnetic field line,

$$\gamma(z) = \gamma_0 + a(z), \quad a = -\frac{e(\Phi - \Phi_0)}{mc^2}, \quad (4)$$

where Φ is the electric potential and $E_{\parallel} = -d\Phi/dz$. Gravitational acceleration (and centrifugal acceleration in the rotating frame) is neglected compared to the electric acceleration.

The electric potential satisfies Poisson equation,

$$\frac{d^2\Phi}{dz^2} = -4\pi(\rho - \rho_{GJ}), \quad (5)$$

where we assumed that the potential varies along z much faster than it does in the transverse directions, i.e. the acceleration length l_{\parallel} is much smaller than the characteristic transverse scale of the problem l_{\perp} , which may be associated with the size of the polar cap. This condition is satisfied for the flows considered below.² The term $-\rho_{GJ}$ may be viewed as a fixed background charge density. The charge density of the flow itself is given by

$$\rho(z) = j_B \int_1^{\infty} \frac{w(\gamma_0) d\gamma_0}{v(\gamma_0, z)}. \quad (6)$$

Here $v(\gamma_0, z)$ is the velocity of particles that start at $z = 0$ with initial Lorentz factor γ_0 ; note that $v^2/c^2 = 1 - \gamma^{-2}$ where $\gamma(z)$ is given by Equation (4). Function $w(\gamma_0)$ describes the probability distribution of γ_0 . The width of this distribution is controlled by the temperature of polar cap T . For example, $w = \delta(\gamma_0 - 1)$ describes a cold polar cap ($T = 0$) where all particles have $\gamma_0 = 1$.

² Alternatively, the additional term $\nabla_{\perp}^2 \Phi$ could be moved to the right-hand side of Equation (5) and included in the effective ρ_{GJ} .

We multiply both sides of Equation (5) by $da/dz = -(e/mc^2)d\Phi/dz$, substitute Equation (6), and find

$$\frac{mc^2}{2e} \frac{d}{dz} \left(\frac{da}{dz} \right)^2 = 4\pi \left[\frac{j_B}{c} \int_1^{\infty} \frac{dp}{dz}(\gamma_0, z) w(\gamma_0) d\gamma_0 - \frac{da}{dz} \rho_{GJ} \right]. \quad (7)$$

On the right-hand side, we used $da/dz = -d\gamma/dz$ (Equation 4) and $d\gamma/v = dp/c$. Integration of Equation (7) in z gives

$$\frac{\lambda_p^2}{2} \left(\frac{da}{dz} \right)^2 = \int_1^{\infty} [p(\gamma_0, z) - p_0] w(\gamma_0) d\gamma_0 - \frac{a(z)}{\alpha}, \quad (8)$$

where

$$p^2(\gamma_0, z) = \gamma^2 - 1 = [\gamma_0 + a(z)]^2 - 1. \quad (9)$$

In Equation (8) we used $a(0) = 0$ and the boundary condition $da/dz(0) = 0$ (the stellar surface is modeled as a perfect conductor that can freely emit charges with $E_{\parallel}(0) = 0$). We also used $j_B(z) \approx \text{const}$ and $\rho_{GJ}(z) \approx \text{const}$, as j_B and ρ_{GJ} do not significantly vary on the characteristic acceleration length λ_p , which is defined by

$$\lambda_p^2 = \frac{mc^3}{4\pi e j_B}. \quad (10)$$

This length may be thought of as the plasma skin depth; it is related to the plasma frequency ω_p ,

$$\lambda_p = \frac{c}{\omega_p}, \quad \omega_p^2 = \frac{4\pi n e^2}{m}, \quad (11)$$

where $n = j_B/ec$ is the characteristic plasma density.

A quick estimate for j_B and λ_p in pulsars may be obtained from the following consideration. The magnetic flux through the polar cap Ψ equals the flux through the light cylinder $R_{LC} = c/\Omega$. The bundle of open field lines is strongly twisted at the light cylinder (toroidal component comparable to poloidal), and hence it carries electric current $I \sim c\Psi/2\pi R_{LC}$, according to Stokes theorem. The current density near the star satisfies $j_B/B \approx I/\Psi$ (which follows from the fact that \mathbf{j} flows along \mathbf{B}); this yields

$$j_B \sim \frac{\Omega B}{2\pi}. \quad (12)$$

Then the plasma skin depth in the polar-cap accelerator may be expressed as

$$\lambda_p \sim \frac{c}{(\Omega\omega_B)^{1/2}}, \quad \omega_B = \frac{eB}{mc}. \quad (13)$$

The scale λ_p is much smaller than the typical size of the polar cap $r_{pc} \sim (R_{NS}^3 \Omega/c)^{1/2}$, where $R_{NS} \sim 10^6$ cm is the radius of the neutron star.

2.2. Cold and warm solutions

Once the injection distribution $w(\gamma_0)$ is specified, it is straightforward to numerically integrate Equation (8) and find $a(z)$. In our sample models we chose $w(\gamma_0) = (kT)^{-1} \exp[-(\gamma_0 - 1)/kT]$ with $kT/mc^2 = 0$ (cold) and 0.03 (warm); the average injection momentum p_0 in the warm model equals $0.22mc$. Figure 1 shows $\Phi(z)$ for the cold and warm solutions.

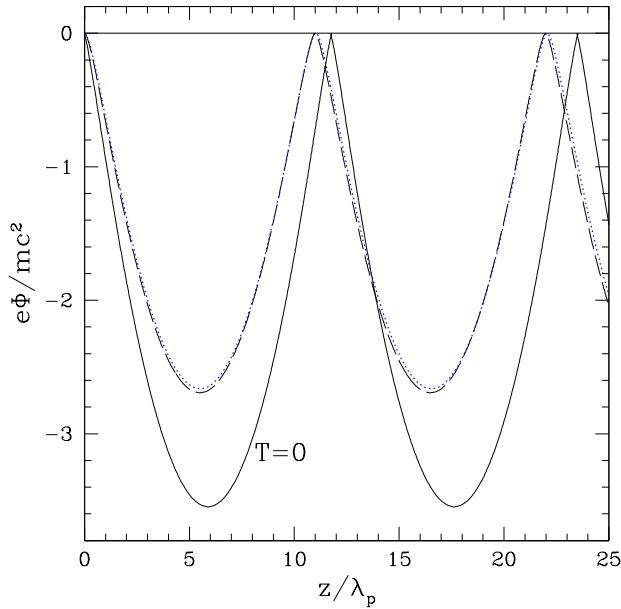


FIG. 1.— Steady-state solution for the charge-separated polar-cap flow with $\alpha = 0.8$. Two cases are shown: cold polar cap $T = 0$ (solid curve) and hot polar cap $kT/mc^2 = 0.03$ (dashed curve), which corresponds to average injection momentum $0.22mc$. Dotted curve shows the solution for a flow where all particles are injected with the same $p_0 = 0.22$.

Figure 1 also shows a third model where all particles injected at the polar cap have $p_0 = 0.22$, i.e. $w(\gamma_0)$ is a delta-function. In this model, Equation (8) simplifies to

$$\frac{\lambda_p^2}{2} \left(\frac{da}{dz} \right)^2 = p(\gamma_0, z) - p_0 + \frac{a(z)}{\alpha}, \quad (14)$$

[same as Equation (3) in B08]. This flow is everywhere cold, i.e. its momentum distribution is described by $f(p') = n \delta[p' - p(z)]$. As one can see in Figure 1, the cold model with $p_0 \neq 0$ provides an excellent approximation to the exact warm model that has the same *average* value of p_0 .

The cold flow solution was discussed in earlier works (Mestel et al. 1985; B08). For $1 - \alpha \ll 1$, the oscillation period is approximately given by (B08)

$$z_0 \approx 2^{3/2} \frac{\lambda_p}{1 - \alpha}, \quad 1 - \alpha \ll 1. \quad (15)$$

The precise period is obtained by numerical integration; e.g. $z_0 = 11.0 \lambda_p$ for $\alpha = 0.8$. The momentum of the steady cold flow $p(z)$ oscillates between the injection momentum $p_0 \ll 1$ and a maximum value p_{\max} . The minima and maxima are where $da/dz = 0$, and from Equation (14) one finds

$$p_{\max} = \frac{2\alpha \gamma_0 - (1 + \alpha^2)p_0}{1 - \alpha^2}. \quad (16)$$

The above equations assumed $\alpha(z) = \text{const}$. In real pulsars, α varies due the field-line curvature and general relativistic effects (Muslimov & Tsygan 1992). The length-scale of this variation $(d\alpha/dz)^{-1}$ is typically larger or comparable to the stellar radius, which exceeds λ_p

by several orders of magnitude. When α varies with z , the analytical integration of the dynamic equation is not possible and one has to solve the two coupled differential equations (B08),

$$\frac{dp}{dz} = \frac{\sqrt{1+p^2}}{pc} \frac{eE_{\parallel}}{mc}, \quad (17)$$

$$\frac{dE_{\parallel}}{dz} = \frac{4\pi j_B}{c} \left(\frac{\sqrt{1+p^2}}{p} - \frac{1}{\alpha(z)} \right) \quad (18)$$

The solution is similar to the case where α is constant, as long as $0 < \alpha < 1$. The momentum $p(z)$ quasi-periodically passes through maxima and minima. The only difference is that the period z_0 and p_{\max} now gradually change with z (see Figure 1 in B08).

2.3. Stability of the flow

Although the cold flow solution with $p_0 = 0.22$ reproduces very well the electric potential $\Phi(z)$ of the exact warm solution with the same average p_0 , the warm and cold flows are qualitatively different. Their different momentum distribution functions $f(p, z)$ leads to a qualitatively different response to small perturbations.

Consider first the cold-flow solution shown by the blue dotted curve in Figure 1. Since all particles are injected with the same momentum $p_0 = 0.22$, all of them follow a single trajectory in the phase space (z, p) . They periodically reach the minimum momentum p_0 at $z_k^* = kz_0$ ($k = 0, 1, \dots$) where potential Φ reaches maximum. There are no particles with momenta $p \approx 0$, so a small perturbation cannot force any particles to reverse their direction of motion, and hence the perturbation will be advected along the flow. This flow is expected to be stable.

In contrast, the warm flow (dashed curve in Figure 1) has a broad distribution of p_0 that extends from $p_0 = 0$. At each peak of the electric potential (at $z = z_k^*$) there is a population of particles with nearly zero velocities. Consider a perturbation at $z \approx z_k^*$. For example, suppose a small bunch \mathcal{A} of particles with momenta in a range $(p_1, p_1 + \Delta p)$ are slightly pushed forward while the rest of particles are unperturbed. This perturbation implies a local increase in electric current $j > j_B$ and hence $\partial E_{\parallel}/\partial t < 0$ (Equation 3), generating negative electric field δE_{\parallel} at $z \approx z_k^*$ that tends to restore the condition $j = j_B$. In contrast to the initial perturbation, the induced δE_{\parallel} affects *all* local particles, regardless of their momenta, not just bunch \mathcal{A} . This has two implications: (1) The induced $E_{\parallel} < 0$ will easily and quickly reduce j back to j_B but will be unable to decelerate bunch \mathcal{A} to the momentum it would have in the steady state flow — bunch \mathcal{A} will continue to move to $z > z_k^*$ with a larger momentum. (2) $\delta E_{\parallel} < 0$ will give very slow particles $p \approx 0$ negative velocities, creating a new bunch \mathcal{B} that slides backward down the potential hill. Bunch \mathcal{B} creates $j < j_B$ at $z < z_k^*$, and the system reacts there by inducing a small $\delta E_{\parallel} > 0$, which accelerates all local particles, regardless their momenta, not just bunch \mathcal{B} . As a result, j quickly recovers to j_B , however, bunch \mathcal{B} is not stopped from moving backward and away from $z = z_k^*$.

One concludes that the perturbation creates a permanent damage to the steady state that broadens the momentum distribution by creating backflowing particles. This perturbation is *not* advected away along the

flow, and can develop further. The backflowing particles turn out to be trapped between two peaks of the electrostatic potential. Further development can be studied with kinetic time-dependent simulations; it eventually completely destroys the steady state solution.

3. NUMERICAL SETUP

Our numerical method is similar to that used by Beloborodov & Thompson (2007, hereafter BT07). The plasma is modeled as a large number $N \sim 10^6$ of individual particles that flow along the magnetic field lines. We assume that the magnetic field is fixed in the co-rotating frame of the star; thus j_B and ρ_{GJ} are fixed. Then the problem becomes essentially one-dimensional, as discussed in detail in BT07. In the present paper, we consider only charge-separated flows, with no pair creation. Three other differences from the magnetar simulation in BT07 are as follows: (1) The magnetar problem had $\alpha \gg 1$ (ρ_{GJ} was negligible compared with j_B/c); in contrast, ρ_{GJ} is crucial for polar-cap flows considered here. (2) The presence of gravity was essential for the closed-field circuit considered in BT07, where the global plasma flow was studied on a scale comparable to the radius of the star; in the problem considered here the electric fields are screened on a much smaller scale $\sim \lambda_p$ and the gravitational acceleration plays no role. (3) The flow behavior on the small scales $z \ll R_{NS}$ may be studied using a small computational box $H \ll R_{NS}$ with an open outer boundary (see below).

In the absence of pair creation, the flow is composed of particles lifted from the surface. In most simulations presented below we assume that all particles have the same mass m and charge e . The particle motion is described by the equation,

$$\frac{dp_i}{dt} = \frac{eE_{\parallel}(z_i)}{mc}, \quad i = 1, \dots, N, \quad (19)$$

where p_i is the momentum of the i -th particle in units of mc , and $E_{\parallel}(z_i)$ is the self-consistent electric field at the particle location z_i . The field is found by integrating Gauss law (Equation 2) along the magnetic field line,

$$E_{\parallel}(z_i) = 4\pi [eN(z_i) - \rho_{GJ}z_i]. \quad (20)$$

Here $N(z_i)$ is the column density of particles between $z = 0$ and $z = z_i$, and we used the boundary condition $E_{\parallel}(0) = 0$, as the material below the stellar surface is assumed to be a very good conductor that can emit free charges. Divergence of the perpendicular component of electric field E_{\perp} is neglected in Equation (20) (see BT07 for discussion of this approximation). The approximation $|\nabla_{\perp} \cdot \mathbf{E}_{\perp}| \ll |dE_{\parallel}/dz|$ is valid if the characteristic scale of the flow acceleration z_0 is smaller than the transverse scale l_{\perp} , which is limited by the polar-cap size r_{pc} ; the condition $z_0 \ll r_{pc}$ is satisfied in the dead-zone models presented below. We also assume that ρ_{GJ} is approximately constant on scale z_0 . Equations (19) and (20) in essence describe a relativistic, time-dependent diode problem with an additional fixed background charge density $-\rho_{GJ}$.

As we track the motion of all particles individually, the continuity equation is automatically satisfied; for a charge-separated flow it is equivalent to charge conserva-

tion,

$$\frac{\partial \rho}{\partial t} + \frac{\partial j}{\partial z} = 0. \quad (21)$$

Equation (3) follows from Equations (2) and (21), so we will not need Equation (3). Instead, the parameter j_B enters the problem as a boundary condition. The magnetic field lines are frozen in the excellent conductor below the stellar surface, which sustains $j(0) = j_B$. This condition is enforced in the simulation by injecting the charges in the computational box at $z = 0$ with the fixed rate j_B (BT07).

The electric current j_B is enforced at one boundary $z = 0$. Since the computational box has a finite size H , we also have to choose a boundary condition at $z = H$ and the value of H . In all sample models shown in this paper we use the simplest boundary condition: particles moving out of the box are lost and no particles enter the box at $z = H$. This condition may be refined by allowing a small inflow of returning particles at the outer boundary. We ran test simulations that show that the refinements are not important as long as the boundary is sufficiently far, so that H is much larger than the characteristic scale of the flow acceleration.

In the one-dimensional model, the transverse gradients are neglected and the flow effectively has a slab geometry. Then it is sufficient to follow particles flowing through a small area A of the slab. This allows one to choose a reasonable number of particles in the computational box, $N \sim AHn$, e.g. $N \sim 10^6$, so that their dynamics can be followed in a reasonable computational time. On the other hand, N should be large enough so that the plasma scale λ_p contains many particles $N_p = A\lambda_p n$.

In summary, we choose N and H so that

$$\frac{H}{\lambda_p} \gg 1, \quad N_p = \frac{\lambda_p}{H} N \gg 1. \quad (22)$$

In this limit, the results are expected to be independent of the choice of N and H (we verified this by varying the two parameters). For most of our simulations $H = 100\lambda_p$ and $N \sim 10^6$. Another requirement is a small time step of the simulation, $\Delta t \ll \omega_p^{-1}$, so that plasma oscillations are well resolved.

4. RESULTS

4.1. Steady state and stability tests

In our simulations and in reality the plasma above pulsar polar caps is collisionless. In the absence of pair creation it must satisfy the Vlasov equation,

$$\frac{\partial F}{\partial t} + \mathbf{v} \cdot \nabla F + \frac{d\mathbf{p}}{dt} \cdot \nabla_{\mathbf{p}} F = 0, \quad (23)$$

where $F(t, z, p)$ is the particle distribution function in phase space. The electric current is $j(t, z) = \rho \bar{v}$ where $\bar{v}(t, z)$ is the average velocity of the particles. As a first simple test, consider a uniform flow with $\rho(z) = \rho_{GJ}$, $\bar{v}(z) = \alpha c$, and $E_{\parallel}(z) = 0$. It is easy to see from Equations (19), (20) and (23) that the flow must remain in this state. This behavior is reproduced by our simulations. The steady uniform flow can have any momentum distribution $F(p)$ as long as $\bar{v} = \alpha c$. Note that it requires a continual injection of particles at $z = 0$ with the average velocity $\bar{v} = \alpha c$ (which also requires $0 < \alpha < 1$).

As a second test, consider a “cold” flow where all particles move with momentum $p(z)$, with zero momentum dispersion. Suppose the flow is injected at $z = 0$ with velocity $v_0 < \alpha c$. Then E_{\parallel} must be generated, accelerating the flow. In a steady state, the solution for the cold flow must have the form, $F(z, p') = n(z) \delta[p' - p(z)]$, where $p(z)$ and $n(z)$ can be described analytically. We first test the special case $\alpha = 1$ (Michel 1974). The flow is accelerated by the self-consistent $E_{\parallel}(z)$, and p exceeds unity at $z \sim \lambda_p$. At heights $z \gg \lambda_p$, velocity approaches c , charge density of the flow $\rho = j_B/v$ approaches ρ_{GJ} , and electric field E_{\parallel} asymptotes to a constant value,

$$E_{\parallel} = \left[\frac{8\pi mc j_B}{e} (\gamma_0 - p_0) \right]^{1/2} [1 + \mathcal{O}(p^{-1})], \quad (24)$$

where $\gamma_0 = (1 - v_0^2/c^2)^{-1/2}$ and $p_0 = \gamma_0 \beta_0$. Then the flow momentum keeps growing linearly with z ,

$$p(z) = [2(\gamma_0 - p_0)]^{1/2} \frac{z}{\lambda_p}, \quad z \gg \lambda_p. \quad (25)$$

This analytical solution is reproduced by our simulations. After an initial relaxation period (comparable to the light crossing time of the computational box) the system forgot initial conditions and relaxed to the steady state shown in Figure 2 (in this example, $v_0 = 1/6$). The charge density of the flow is large near the polar cap surface and asymptotes to ρ_{GJ} at $z \gg \lambda_p$, as expected.

Then we studied cold flows with $0 < \alpha < 1$ with a fixed injection velocity β_0 . We chose in our sample numerical model $\alpha = 0.8$ and $\beta_0 = 0.2$. The computational box was initially empty; the plasma injected at $z = 0$ filled the box on the dynamical timescale $\sim H/c$ and established a steady state shown in Figure 3. The steady state is in perfect agreement with the analytical model of Section 2. The charge density $\rho(z)$ has spikes at $z = kz_0$ ($k = 0, 1, \dots$) where the flow has the minimum velocity β_0 ; the height of each spike is $\rho_{\max} = j_B/\beta_0 = (\alpha/\beta_0)\rho_{GJ}$. The charge spikes are associated with maxima of the electric potential (Figure 3c). The oscillating momentum has maxima $p_{\max} = 3.6$, in excellent agreement with Equation (16). The period of oscillation is $z_0 \approx 11\lambda_p$, same as found using the method of Section 2.

As anticipated in Section 2.3, we find that the steady state becomes unstable if we reduce β_0 to zero. Then any small perturbation (e.g. due to numerical error) completely destroys the steady state; instead, a time-dependent state forms, with a broadened momentum distribution function. A steady flow with a finite $\beta_0 \neq 0$ can also be destroyed, although in this case a finite, sufficiently large perturbation is required. In fact, this case provides a better setup for a numerical analysis of the instability, as we can control the form of the initial perturbation and then observe how it destroys the flow that was stable before the perturbation was applied. We made such an experiment with the flow with $\alpha = 0.8$ and $\beta_0 = 0.2$. We applied a perturbation that was localized in space and time — a small “kick” δp was given to all particles located in a small region $\delta z = \lambda_p/2$; in this experiment δp had a Gaussian distribution with the mean value and dispersion equal to 0.02. We observed the following evolution. As the localized perturbation moved along with the background flow, it was greatly amplified when

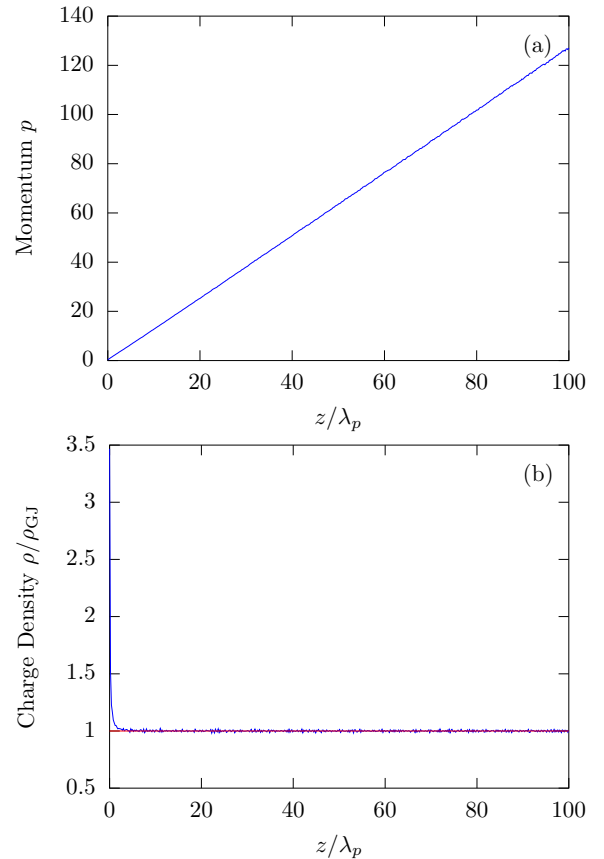


FIG. 2.— Test run for a cold-flow model with $\alpha = 1$ and $v_0 = c/6$. The flow relaxed to a steady state in the entire box $H = 10^2 \lambda_p$ on the light-crossing timescale, H/c ; the state of the system is shown at $t = 10H/c$. (a) Flow momentum per particle $p(z)$ in units of mc . (b) Charge density $\rho(z)$ in units of ρ_{GJ} .

it reached the potential maximum (which corresponds to the minimum $p_0 \approx 0.2$ of the steady-state solution, see Figure 3), and some particles acquired a negative momentum, i.e. reversed their direction of motion. Most of the reversed particles became trapped between two potential maxima, and some of them were able to penetrate even further back, beyond the preceding potential peak. The perturbation further spread in the phase space and the damage to the initial steady-state solution was further amplified with time, in particular near the potential maxima. Eventually, the entire flow became strongly time-dependent and the regular periodic structure of potential peaks disappeared.

The amplification of small (linear) perturbations at the potential maximum can be understood as follows. Consider a particle whose Lorentz factor differs from that of the background cold flow by a small $\delta\gamma$. As the particle moves along with the flow, its deviation $\delta\gamma$ remains constant, because it travels in the same electrostatic potential of the background flow (cf. Equation 4). Using the relation $d\gamma/dp = \beta$, we find the perturbation of momentum δp that corresponds to $\delta\gamma$,

$$\delta p = \frac{\delta\gamma}{\beta} \propto \beta^{-1}. \quad (26)$$

It grows as the particle (and the background flow) de-

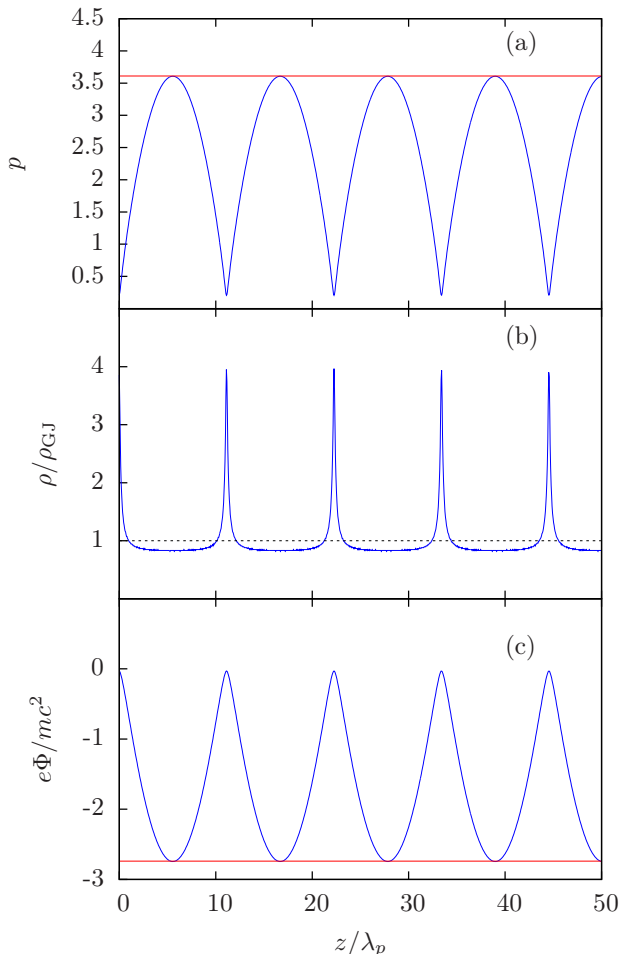


FIG. 3.— Cold flow with $\alpha = 0.8$ and $\beta_0 = 0.2$ at time $t = 1.45H/c$ (a) Momentum p (in units of mc). Red line shows the maximum value predicted by Equation (16). (b) Charge density. (c) Electrostatic potential. Red line shows the minimum value predicted by the analytical model of Section 2.

celerates near the potential maximum; the corresponding amplification factor β_0^{-1} is particularly large if β_0 is small.

The generation of backflowing particles at the potential peaks z_k^* plays a key role in disrupting the steady state. We also observe that, in a flow with a finite minimum velocity $\beta_0 > 0$, only a finite, sufficiently large perturbation can destroy the steady state. The perturbation would need to steal from particles energy $\gamma_0 - 1 \approx \beta_0^2/2$ so that they can be reflected by the potential hill. The energy gap $\gamma_0 - 1$ stabilizes the flow against infinitesimal perturbations, and only a sufficiently strong kick disrupts the flow.

The trapped/backflowing particles have a deteriorating effect on the steady state because they are not advected away with the flow and instead repeatedly approach the same potential peaks, amplifying the perturbations. In addition, one can view the trapped particles as extra charge that distorts the electric field. Let N_{trap} be the number of particles trapped between two potential peaks z_{k-1}^* and z_k^* ; they create electric field $E' = 4\pi e N_{\text{trap}}$ at $z > z_k^*$. The corresponding distortion of the electrostatic potential $\Phi' = -E'z$ grows linearly with z and

becomes significant at sufficiently large z even if N_{trap} is small. The distance z required to produce $e\Phi' \sim mc^2$ is $z \sim (N_p/N_{\text{trap}})\lambda_p$. This behavior is qualitatively confirmed by our numerical experiments with larger simulation boxes H — the flow was found to become more unstable with increasing H .

4.2. Time-dependent state with warm particle injection

In a more realistic model, particles are lifted from the polar cap with a thermal velocity dispersion $\Delta v_0 \sim v_0$. The flow still starts with a small velocity $\bar{v} \ll c$ and hence with a large charge density $\rho \gg \rho_{\text{GJ}}$, which self-consistently generates the accelerating electric field. The basic acceleration mechanism is the same as for the cold flow shown in Figures 2 and 3. However, there is a new feature: particles with different initial velocities behave differently in the collective electric potential, and the charge density $\rho(z)$ is changed from the cold-flow solution, even though $\Delta v_0 \ll c$. Some particles have $v \approx 0$ and can reverse their motion in the regions of growing potential ($E_{\parallel} < 0$), which greatly complicates the behavior of the distribution function $F(z, p)$.

In our simulations, we modeled the warm injection by a one-dimensional Maxwell distribution, which is a simple Gaussian with dispersion Δv_0 equal to the mean value \bar{v}_0 ; we chose $\bar{v}_0 = 0.2c$. As initial conditions we took the steady-state solution (Section 2). The main parameter of the flow is α , and we performed simulations for several values of α in the range $0 < \alpha < 1$.

As expected, the steady state was quickly destroyed and the flow kept oscillating in space and time. The basic parameters of the flow remained, however, similar to the steady cold model. The average charge density (averaged over oscillations) is nearly equal to ρ_{GJ} and the average velocity \bar{v} is nearly equal to αc , so that the condition $j = j_B$ is satisfied. Figure 4 shows the evolution of the hydrodynamic velocity $\bar{v}(t)$ measured at a fixed location z_1 (we chose $z_1 = 50\lambda_p$, in the middle of the computational box; \bar{v} was calculated by averaging over particles inside a small bin around z_1 , of width $2\lambda_p$). The hydrodynamic velocity $\bar{v}(t)$ oscillates around αc ; these oscillations have a relatively small amplitude $\delta v \ll \bar{v}$.

The moderate value of the hydrodynamic velocity does not, in principle, exclude acceleration of a fraction of particles to much higher energies. We therefore also studied the momentum distribution of particles in the flow. Figure 5a shows a random snapshot of the particle distribution in the phase space for the flow with $\alpha = 0.8$. We randomly chose 1000 particles between $z = 0$ and $z = 100\lambda_p$ and the figure shows their locations in the two-dimensional phase space (z, p) . The simulation demonstrates the following:

(1) There is no high-energy tail in the momentum distribution.

(2) At each z , the momentum distribution has a pronounced narrow peak at p_{peak} . Thus, a large fraction of particles form a cold stream; this fraction is approximately equal to α (see below). The momentum of the cold stream p_{peak} is above (but comparable to) p_{max} predicted by the steady-state model.

(3) There is a low-energy wing in the momentum distribution which extends to negative momenta. This broad component of the particle distribution has a hydrody-

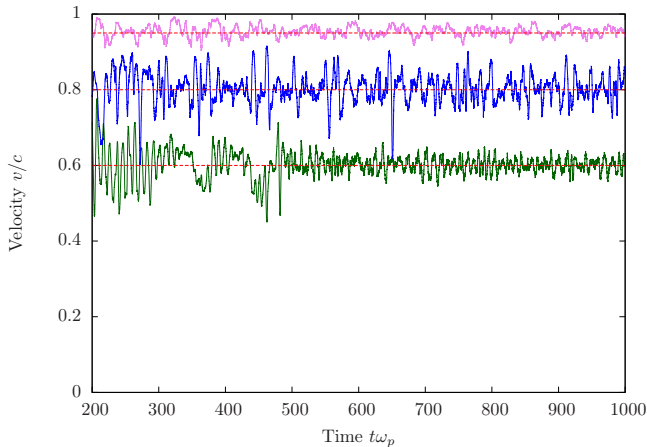


FIG. 4.— Evolution of the hydrodynamical velocity \bar{v} of the flow measured in the middle of the computational box. Three models are shown: $\alpha = 0.95$ (purple), 0.8 (blue) and 0.6 (dark green). In all three cases, the time-average value of \bar{v} equals α (red horizontal lines).

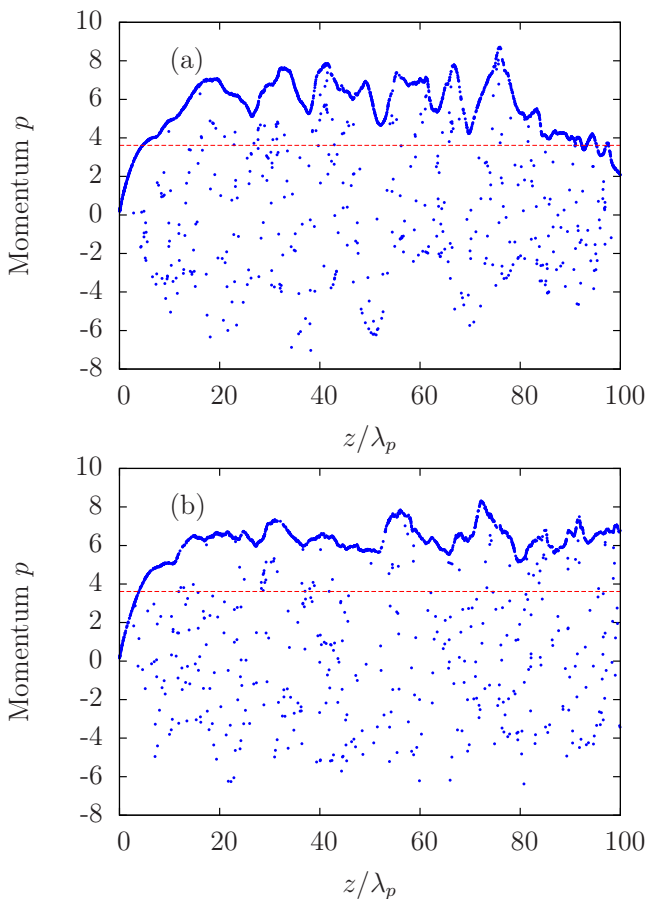


FIG. 5.— Snapshot of 1000 randomly chosen particles in phase space for the flow with $\alpha = 0.8$ and $\beta_0 = 0.2$. Red dashed line shows the maximum momentum p_{\max} for the steady cold solution with the same $\alpha = 0.8$ and $\beta_0 = 0.2$. (a) Random snapshot for the simulation with box size $H = 100\lambda_p$. (b) Another random snapshot of a similar simulation with a larger computational box $H = 200\lambda_p$.

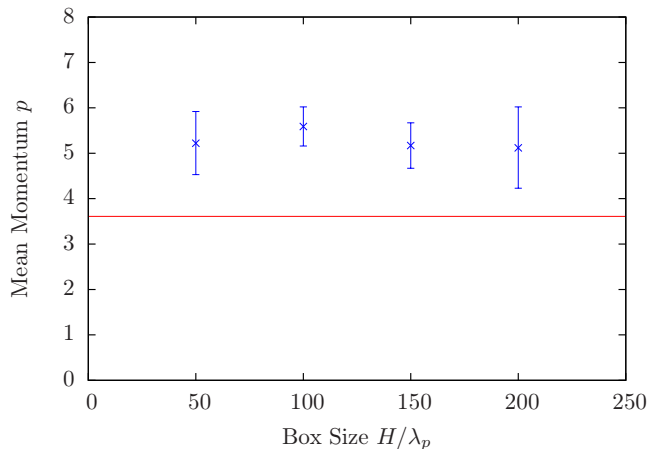


FIG. 6.— Mean expectation and standard deviation for the fluctuating hydrodynamical momentum of the flow measured at the center of the computational box. Four simulations are shown, with box sizes $H/\lambda_p = 50, 100, 150,$ and 200 ; all four simulations have the same parameter $\alpha = 0.8$. Red line shows the maximum momentum predicted by the steady state model with $\alpha = 0.8$.

dynamic velocity close to zero; these particles are “trapped” and do not contribute much to the current density; however they make a significant contribution to charge density. In our sample model, about 20% of particles reside in the broad trapped component, and this fact has a simple explanation. From the point of view of the cold stream dynamics, the broad component provides a background that offsets the effect of vacuum charge density ρ_{GJ} by the fraction of 20%. This fraction approximately equals to $1 - \alpha$, so that the other particles (fraction $\approx \alpha$) may move in the cold stream with $v \approx c$ and carry j_B without the mismatch in charge density that would generate strong E_{\parallel} . In essence, the broad component with backflowing particles allows the plasma to self-organize so that the cold stream can keep $v \approx c$. This is in contrast to the steady-state solution in Section 2 where all particles formed a stream with a positive velocity $v \neq \alpha$, which must be periodically decelerated and accelerated.

(4) The cold stream momentum p_{peak} fluctuates in time (the corresponding curve in Figure 5 moves in time). However, the qualitative form of the phase-space distribution remains similar to that in Figure 5.

As seen in Figure 5a, the flow momentum p_{peak} decreases near the outer boundary of the computational box $z = H$. This is an artifact of the boundary condition (free escape with no backflow), which suppresses the density of backflowing particles near the boundary. As a result, a modest negative electric field is induced near the boundary, decreasing p_{peak} so that the flow carries the required electric current j_B . For comparison, Figure 5b shows a random snapshot of a similar model (in the same interval $0 < z < 100\lambda_p$) that has twice as large computational box, $H = 200\lambda_p$. As we increase H , the boundary effect moves away to larger z , affecting the flow properties only at $z \approx H$. The flow structure inside the box (away from the boundary) does not depend on H .

To check whether the flow momentum depends on the size of the computational box, we ran several simulations with the same $\alpha = 0.8$ and different box sizes H . In each simulation, we measured the fluid momentum \bar{p} in the center of the box (using a bin $\Delta z = 2\lambda_p$) at time

$t = 100\omega_p^{-1}$. The results are shown in Figure 6. There is no systematic variation in \bar{p} with the box size; the small variations ($\lesssim 10\%$) are consistent with the fluctuations of \bar{p} in time for each model.³

The polar-cap flows in pulsars extend through altitudes z much larger than our box size H . The fact that our results are independent of H confirm the expected behavior — the plasma keeps oscillating and particle acceleration is quenched everywhere as long as the flow satisfies the condition $0 < \alpha < 1$. We observe a quasi-uniform and quasi-steady behavior in the computational box (apart from the initial acceleration region of length $\sim 10\lambda_p$). In a realistic polar-cap flow, each segment of length $\sim 100\lambda_p$ should behave like our computational box.

We also ran simulations with varying $\alpha(z)$. We ran models with $d\alpha/dz \sim 2 \times 10^{-4}\lambda_p^{-1}$ (realistically, $d\alpha/dz$ should be even smaller, $d\alpha/dz \lesssim R^{-1}$, where R is the star radius). The results are similar to the case of $\alpha = \text{const}$. The maximum momentum remains comparable to that given by Equation (16) as long as $0 < \alpha < 1$.

5. MIXED ION FLOW AND TWO STREAM INSTABILITY

If $j_B > 0$ (which is equivalent to $\rho_{GJ} > 0$ for $\alpha > 0$), the charge-separated flow puled out from the polar cap is made of ions. Different ion species may end up in such a flow, and they will be accelerated to different velocities.

The mixed ion flow shares many features with the identical-particle model studied in the previous sections. Steady state solutions can be obtained using the method described in Section 2. Ions with different masses and charges move with different hydrodynamical momenta and co-exist in a common, periodic electrostatic potential. This steady solution is prone to kinetic instability similar to that described in Sections 2 and 4. There is, however, an important new feature: the ion streams with different hydrodynamical momenta are prone to two-stream instability.

To study the behavior of the mixed ion flow we slightly change the setup of our numerical simulation. Consider, e.g., a mixture of protons and helium nuclei (alpha-particles). The particle injection at $z = 0$ now consists of two ions species; they have charges e_1 and $e_2 = 2e_1$, and masses m_1 and $m_2 = 4m_1$. The two species are injected with equal rates $\dot{N}_1 = \dot{N}_2$. Then alpha-particles carry electric current $j_2 = e_2\dot{N}_2$ that is two times larger than the proton current $j_1 = e_1\dot{N}_1$. Thus, $j_2 = (2/3)j_B$ and $j_1 = (1/3)j_B$ are maintained at the boundary.

To define a characteristic plasma skin depth λ_p we use Equation (10) where we replace e, m, j_B by (e_1, m_1, j_1) or, equivalently, by (e_2, m_2, j_2) (note that $e_2j_2/m_2 = e_1j_1/m_1$). The characteristic plasma frequency is defined by $\omega_p = c/\lambda_p$.

Figure 7 shows a snapshot of the phase-space distribution of ions long after the beginning of the simulation. In this sample model $\alpha = 0.4$. The modest value of α (not

³ Note that the average momentum \bar{p} does not correspond to the average velocity \bar{v} shown in Figure 4, in the sense that $\bar{p} \neq \bar{\beta}(1 - \bar{\beta}^2)^{-1/2}$, because of the broad low-energy tail of the distribution function. Compared with \bar{v} , the calculation of \bar{p} gives a higher weight to fast particles due to the additional factor γ in $p = \gamma\beta$. The average velocity remains close to αc , and the averaged momentum is larger than $\bar{\beta}(1 - \bar{\beta}^2)^{-1/2}$.

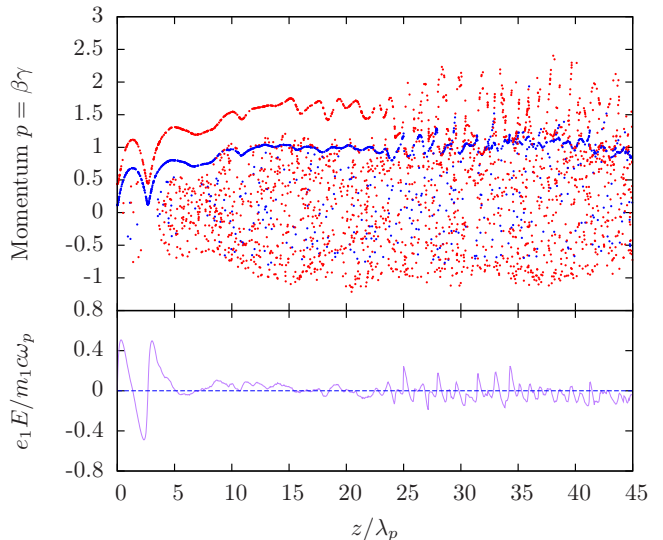


Fig. 7.— Snapshot of the mixed ion flow with $\alpha = 0.4$ at time $t = 10^3\omega_p^{-1}$. Top panel shows the phase space distribution, where red dots represent protons and blue dots represent helium ions. Bottom panel shows the electric field.

close to unity) implies modest Lorentz factors of particles and the fast development of instabilities. The flow exhibits the following features:

- (1) One period of the steady state solution is reproduced near the injection boundary $z = 0$. The period $z_0 \approx 3\lambda_p$ agrees with the result from numerical integration of the corresponding steady state model. (This feature is stable in our sample model because we chose a high injection velocity $v_0 \approx 0.4c$.)
- (2) At larger z the periodic flow becomes unstable and develops into a configuration similar to that in Figure 5, except that now we have *two* cold variable streams. Besides the cold streams, there is a broad distribution of ions with smaller momenta and a negligible hydrodynamic velocity. The origin of this broad component of trapped particles was discussed in Section 4.2 and plays here a similar role — it is self-organized so that the streams may move with a relativistic speed without a mismatch in charge density.
- (3) Further from the boundary (at $z > 20\lambda_p$), the two streams develop a two-stream instability. The growth rate of the instability may be estimated using an idealized model of two cold fluids with densities n_1, n_2 and velocities v_1, v_2 . It is straightforward to derive the dispersion relation for Langmuir modes with frequency ω and wave-vector k (e.g. Melrose 1986); it gives,

$$1 - \frac{\omega_1^2}{\gamma_1^3(\omega - kv_1)^2} - \frac{\omega_2^2}{\gamma_2^3(\omega - kv_2)^2} = 0, \quad (27)$$

where $\omega_1^2 = 4\pi n_1 e_1^2 / m_1$ and $\omega_2^2 = 4\pi n_2 e_2^2 / m_2$. Using $\omega_1 \approx \omega_2 \approx \omega_p$ and the characteristic values of velocities v_1, v_2 from our simulation, we find from Equation (27) that the most unstable modes have ω comparable to ω_p and their growth rate is $\Gamma \sim 0.2\omega_p$. In the simulation we observe a slightly smaller Γ . The distance over which the Langmuir waves are amplified is roughly $10\lambda_p$. As a result of the instability, the two streams are smeared out at large z , in particular the stream of lighter ions. No

significant particle acceleration is seen in the simulation.

6. DISCUSSION

We have presented detailed one-dimensional time-dependent simulations of the plasma flow extracted from the polar caps of neutron stars. The simulations provide a fully kinetic description of the flow, with self-consistent electric field and particle distribution function. In this paper, we focused on the regime $0 < \alpha < 1$, where α is the main parameter of the flow defined by Equation(1). In agreement with the estimates of B08, we find that the particles are accelerated to Lorentz factors,

$$\gamma \approx \frac{1 + \alpha^2}{1 - \alpha^2}, \quad (28)$$

and are not capable of igniting pair creation. In this sense, flows with $0 < \alpha < 1$ are “dead.” They are sustained by a modest voltage, oscillating in space and time. Although the simulation is limited to regions close to the pulsar surface, the result does not depend on the simulation box size, and hence should describe the entire polar cap flow, as long as α remains between 0 and 1. The parameter α is expected to vary along the magnetic field lines, on a scale comparable to the stellar radius; we have verified that this variation does not change the oscillating behavior of the flow (see also B08).

The simulations show how a kinetic instability develops and disrupts the ideal periodic structure found in the analytical models of the dead zone; the instability mechanism is described in Sections 2 and 4. We find that the momentum distribution function has two distinct parts — a variable “cold stream” and a broad wing at low momenta, which includes particles flowing backward to the polar cap. The fraction of particles in the cold stream is approximately equal to α ; the remaining fraction $1 - \alpha$ forms the broad component. Even though the flow is turbulent, it shows no signs of particle acceleration to energies higher than that of the cold stream.

The value of parameter α depends on the location and geometry of the polar cap. A simplest magnetospheric configuration is that of a centered dipole. Then the parameter α depends on the angle between the magnetic and spin axes, ξ ; besides, it varies across the polar cap. For nearly aligned rotators ($\xi \approx 0$), $0 < \alpha < 1$ in the central part of the polar cap and $\alpha < 0$ in a ring-shaped zone near the edge of the polar cap (Timokhin 2006; Parfrey et al. 2012). In this case, the dead zone occupies the central part of the polar cap, and e^\pm discharge must be confined to the ring, matching the phenomenological “hollow cone” model of pulsar emission. In contrast, the polar cap of an orthogonal rotator ($\xi \approx \pi/2$) has $|\alpha| \gg 1$, which enables e^\pm discharge for the entire polar cap. At arbitrary misalignment $0 < \xi < \pi/2$, the values of α are provided by global three-dimensional simulations of the magnetospheric structure (e.g. Spitkovsky 2006) and should play a key role for the geometry of the radio beam.

We presented our results using plasma skin depth λ_p as a unit of length and particle rest-mass mc^2 as a unit of energy. In this form, the results do not depend on the charge or mass of the particles extracted from the polar cap, as long as the flow is made of identical particles. In particular, Equation (28) is valid for both electron flow ($\rho_{GJ} < 0$) and ion flow ($\rho_{GJ} > 0$), and

the phase-space distribution shown in Figure 5 describes both cases. Note that the accelerating voltage is proportional to the particle mass; voltage implied by Equation (28) is different for ions and electrons by the factor of $m_i/m_e \sim 2 \times 10^3$. The relatively high voltage in the ion flow, $e\Phi \approx m_i c^2 (1 + \alpha^2)/(1 - \alpha^2)$ is still hardly sufficient to ignite e^\pm pair discharge by a seed electron or positron.

The identical-particle model may not hold for an ion flow; in this case, new effects may enter the problem. Firstly, heavy ions pulled out from the polar cap may not be completely ionized and begin to lose electrons as they are accelerated and interact with the X-rays above the stellar surface; this process effectively creates new charges, reminiscent of pair creation (e.g. Jones 2012). Secondly, the ion flow may be a mixture of different nuclei which will be accelerated to different Lorentz factors. The mixed ion flow is prone to two-stream instability, possibly leading to formation of plasma clumps and generation of coherent radio emission. In our simulations, we observe the expected two-stream instability, however do not observe significant structure (clumps) in the turbulent flow. This may change in three-dimensional simulations. The frequency of excited waves (comparable to the ion plasma frequency) is in the radio band, and coherent emission from clumps could create bright coherent emission. It remains to be seen whether this mechanism can contribute to the pulsar emission. If it does, it would create an additional component of the radio pulse. In the case of approximately aligned rotator, the additional component would be generated in the central region of the polar cap, leading to a “hollow cone + core” structure of the radio pulse.

The charge-separated model of the dead zone can be modified to include possible backflowing particles from distant parts of the open field-line bundle (e.g. from a pair-producing outer gap). These particles can contribute to the current density and also serve as an additional background charge density, which may be modeled as a contribution to the effective “vacuum” charge density $-\rho_{GJ}$. This would change the effective α (Lyubarsky 1992; B08), most likely reducing it.

An outer gap is expected to form in a charge-separated flow near the null surface $\vec{B} \cdot \vec{\Omega} = 0$ (Cheng et al. 1986). On a given field line, the outer gap will be screened if it is loaded by multiple e^\pm pairs produced by the discharge at the polar cap. Thus, the suppression of e^\pm discharge near the field-line footpoint is an essential condition for the existence of an outer-gap accelerator. Therefore, one can expect an outer gap to form on field lines with footpoints in the dead zone.

We did not simulate in this paper flows with $\alpha > 1$ or $\alpha < 0$; in these cases particles must be strongly accelerated. This regime leads to e^\pm discharge that must be unsteady, with a significant intermittent backflow (B08). A model for oscillating discharge may be constructed in hydrodynamical approximation (Levinson et al. 2005), however a fully kinetic description is essential, as demonstrated by our results for the dead zone, where a significant fraction of particles are trapped and form a broad wing at low momenta in the distribution function. The discharge simulation can be done using our setup of a fixed current $j = j_B$ at the stellar surface (BT07) and

incorporating pair creation. We defer the simulations with $\alpha > 1$ and $\alpha < 0$ to a future work.

When this work was completed, the preprint by Timokhin & Arons (2012) came out. They present simulations of charge separated flows, using a similar method, and the results agree with our results for $0 < \alpha < 1$. They

also consider flows with $\alpha < 0$ and $\alpha > 1$, and find a strong unsteady e^\pm discharge confirming the analysis in B08.

This work was supported by NASA NNX10AI72G.

REFERENCES

- Arons, J., & Scharlemann, E. T. 1979, *ApJ*, 231, 854
 Beloborodov, A. M. 2008, *ApJ*, 683, L41
 Beloborodov, A. M., & Thompson, C. 2007, *ApJ*, 657, 967
 Cheng, K. S., Ho, C., & Ruderman, M. 1986, *ApJ*, 300, 500
 Fawley, W. M., Arons, J., & Scharlemann, E. T. 1977, *ApJ*, 217, 227
 Goldreich, P., & Julian, W. H. 1969, *ApJ*, 157, 869
 Jones, P. B. 2012, *MNRAS*, 419, 1682
 Kennel, C. F., Fujimura, F. S., & Pellat, R. 1979, *Space Science Reviews*, 24, 407, 10.1007/BF00172211
 Levinson, A., Melrose, D., Judge, A., & Luo, Q. 2005, *ApJ*, 631, 456
 Lyubarskij, Yu. E. 1992, *A&A*, 261, 544
 Melrose, D. B. 1986, *Instabilities in Space and Laboratory Plasmas*
 Mestel, L., Robertson, J. A., Wang, Y.-M., & Westfold, K. C. 1985, *MNRAS*, 217, 443
 Muslimov, A. G., & Tsygan, A. I. 1992, *MNRAS*, 255, 61
 Parfrey, K., Beloborodov, A. M., & Hui, L. 2012, *MNRAS*, 423, 1416
 Ruderman, M. A., & Sutherland, P. G. 1975, *ApJ*, 196, 51
 Spitkovsky, A. 2006, *ApJ*, 648, L51
 Sturrock, P. A. 1971, *ApJ*, 164, 529
 Timokhin, A. N. 2006, *MNRAS*, 368, 1055
 Timokhin, A. N., & Arons, J., 2012, submitted to *MNRAS*, (arXiv:1206.5819)